Received 12 March 2023; revised 13 April 2023; accepted 28 April 2023. Date of publication 2 May 2023; date of current version 9 May 2023.

Digital Object Identifier 10.1109/OJAP.2023.3272570

Fully Printed 3-D Antennas With Wideband Radiation Isotropy Based on Annular Currents Models

RUIQI WANG, KIRILL KLIONOVSKI, AND ATIF SHAMIM (Senior Member, IEEE)

CEMSE, King Abdullah University of Science and Technology, Thuwal 23955, Saudi Arabia

CORRESPONDING AUTHOR: R. WANG (e-mail: ruiqi.wang.1@kaust.edu.sa).

This work was supported by the CEMSE Division at King Abdullah University of Science and Technology, Kingdom of Saudi Arabia under Grant BAS/1622/01-01.

ABSTRACT Internet of Things (IoT) devices require orientation insensitive communication and a small footprint. Wireless communication should be maintained across the whole operation band, hence electrically small antennas (ESAs) with wideband radiation isotropy are also desired. This paper proposes a theoretical model based on annular ring currents to synthesize quasi-isotropic antenna radiation patterns. The theoretical model shows that wideband radiation isotropy can be achieved by optimizing the combination of azimuthal currents. We subsequently present spherical and cubical ESA designs that achieve measured wide impedance and radiation isotropy bandwidths exceeding 10% for the GSM900 band. The ESAs were fully printed, with substrates 3D printed and metallization applied using screen printing. Despite the electrically small sizes and low cost fully printed fabrication, the antennas achieved approximately 90% radiation efficiencies. The proposed designs are low cost because of additive manufacturing, can have embedded electronics because of their 3D structure and have the largest radiation isotropy bandwidth for an electrically small antenna in published literature.

INDEX TERMS Azimuthal current rings, electrically small antennas, Internet of Things, antenna miniaturization, printing, quasi-isotropic radiation patterns, antenna synthesis theory, wideband antennas.

I. INTRODUCTION

ANTENNAS with quasi-isotropic radiation patterns are attracting considerable research attention because they can provide orientation insensitive communication for Internet-of-Things (IoT) devices as well as generally reduce wireless communication interruptions [1], [2], [3]. These antennas are also attractive for energy harvesting, radio frequency identification (RFID) [4], flood monitoring [5], marine animal monitoring [6], etc. The huge volume of IoT devices requires antennas to be compact and minimal cost, which can both be fulfilled with three-dimensional (3D) antenna-in-package (AiP) and additive manufacturing technologies [7]. The global system for mobile communication (GSM) frequency band is commonly preferred for IoT network connection due to its widespread global infrastructure [8]. The GSM900 band operational bandwidth = 880.0 – 915.0 MHz for uplink and 925.0 – 960.0 MHz for downlink, hence antennas need to maintain their isotropic radiation pattern across the entire 8.7% bandwidth. In the literature, most previous designs have focused on antenna isotropy only at a single frequency without considering the isotropic radiation within a bandwidth [2], [3], [4], [5], [6], [7], and their reported impedance bandwidth is also narrow (< 9%). While some designs aimed at dual-band operation [1], [9], [10], [11], [12]. However, either they have a narrow radiation isotropy bandwidth (< 3%) in each band [9], [10], or the gain variation is larger than 7 dB [1], [11], [12]. Therefore, designing antennas with wideband radiation pattern isotropy is challenging.

One of the most commonly used methods for designing the antennas with quasi-isotropic radiation patterns is to combine electric and magnetic dipoles with a phase difference between them [13], [14], [15], [16], [17], although quasi-isotropic radiation patterns can be synthesized by a linear and slot antenna [18], U-shaped antenna [19], triple current sources [20], and multiple electric dipoles [1], [2], [21]. However, these designs produce narrow radiation isotropy bandwidths. A proposed antenna with four L-shaped monopoles has been reported [22], [23], where one utilized distributed phase shifters [22], and the other a lumped components based phase shifter [23]. Although the radiation pattern isotropy bandwidth (–7 dB from the radiation

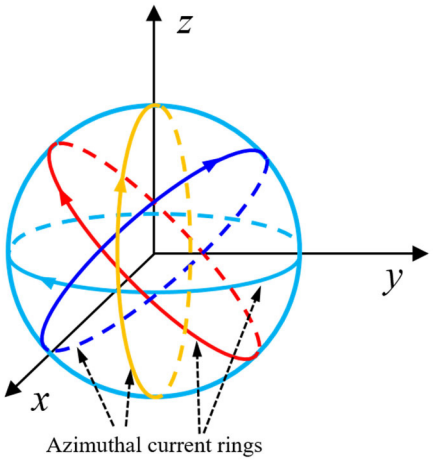

FIGURE 1. Quasi-isotropic antenna synthesis on a sphere using azimuthal current rings.

peak pattern) was acceptable (11.5% and 6%, respectively), the antennas were electrically large; and incorporated planar designs, which are unsuitable for AiP concepts, and hence could not embed electronics within the antenna structure. Finally, the antennas were realized with standard subtractive manufacturing technologies, which also makes them unsuitable for IoT applications where high throughput and low cost manufacturing is required. On the contrary, additive manufacturing, such as the fully printed fabrication process, for the design of high-performance antennas is attractive and promising, which is low-cost and avoids material wastage [5], [6], [7]. Specifically, the antenna substrates can be 3D printed, while the metallic pattern could be realized through screen printing or inkjet printing. Therefore a fully printed fabrication process for antenna design can be achieved for low-cost and mass manufacturing [1], [3].

Thus, this paper proposes a theoretical approach to synthesize antennas with wide radiation isotropy bandwidth, as shown in Fig. 1, incorporating multiple azimuthal electric current rings. Two azimuthal current rings with 90° phase shift provide optimum radiation isotropy performance (2.1 dB gain variation). Analytical results were validated by full-wave simulations. We subsequently fabricated 3D electrically small antennas (ESAs) following the proposed radiation isotropy synthesis theory, achieving current best-practice wide impedance and radiation isotropy bandwidths for GSM900 band. The antennas were fully printed and achieved approximately 90% radiation efficiency.

II. ANALYTICAL MODEL

Consider an annular azimuthal electric current $\mathbf{j}_e^{\varphi}$ of radius a located in the xy-plane in free space, as shown in Fig. 2(a), which can be expressed in cylindrical coordinates (ρ, φ, z) as:

$$\mathbf{j}_e^{\varphi}(\rho, \varphi, z) = I_e^{\varphi}(\varphi)\delta(\rho - a)\delta(z)\boldsymbol{\varphi}_0. \tag{1}$$

where $I_e^{\varphi}(\varphi)$ is the magnitude of the azimuthal electric current, $\delta(z)$ is the Dirac delta function, and $\boldsymbol{\varphi}_0$ is the unit

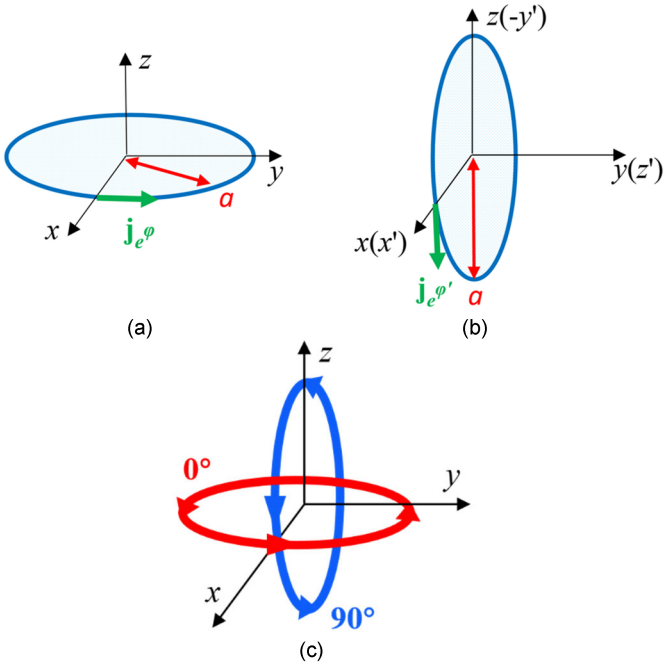

FIGURE 2. Annular current in the (a) xy-plane and (b) xz-plane, and (c) combined current.

azimuthal vector. Meridional E_θ and azimuthal E_φ electric field intensity vector components for the radiation pattern from the annular current can be expressed in the spherical coordinate system (r, θ, φ) as [24]:

$$E_\theta(r, \theta, \varphi) = -\frac{iaZ_0}{2\lambda}\left[D_x \cos\theta \cos\varphi + D_y \cos\theta \sin\varphi\right]\frac{e^{-ikr}}{r},$$
$$E_\varphi(r, \theta, \varphi) = \frac{iaZ_0}{2\lambda}\left[D_x \sin\varphi - D_y \cos\varphi\right]\frac{e^{-ikr}}{r}. \tag{2}$$

where i is the imaginary unit, λ is the wavelength, and $Z_0 = 120\pi$. The expressions for parameters D_x and D_y are:

$$D_x = -\int_{-\pi}^{\pi} I_e^{\varphi}(\varphi_e) e^{i\frac{2\pi}{\lambda}a\sin\theta\cos(\varphi-\varphi_e)} \sin\varphi_e d\varphi_e,$$
$$D_y = \int_{-\pi}^{\pi} I_e^{\varphi}(\varphi_e) e^{i\frac{2\pi}{\lambda}a\sin\theta\cos(\varphi-\varphi_e)} \cos\varphi_e d\varphi_e. \tag{3}$$

Let us rotate the annular current $\mathbf{j}_e^{\varphi}$ to locate in the xz-plane ($x'y'$-plane) (Fig. 2(b)), expressed as (ρ', φ', z') in the cylindrical coordinate system corresponding to Cartesian coordinates (x', y', z'):

$$\mathbf{j}_e^{\varphi'}(\rho', \varphi', z') = I_e^{\varphi}(\varphi')\delta(\rho' - a)\delta(z')\boldsymbol{\varphi}_0'. \tag{4}$$

Meridional and azimuthal components of the radiation pattern from the rotated annular current can be expressed in the spherical coordinate system (r', θ', φ') corresponding to the Cartesian coordinates (x', y', z') as:

$$E_{\theta'}(r', \theta', \varphi') = -\frac{iaZ_0}{2\lambda}\left[D_{x'} \cos\theta' \cos\varphi' + D_{y'} \cos\theta' \sin\varphi'\right]\frac{e^{-ikr'}}{r'},$$
$$E_{\varphi'}(r', \theta', \varphi') = \frac{iaZ_0}{2\lambda}\left[D_{x'} \sin\varphi' - D_{y'} \cos\varphi'\right]\frac{e^{-ikr'}}{r'}. \tag{5}$$

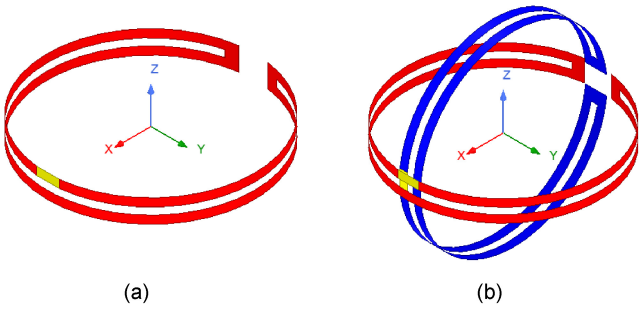

FIGURE 3. (a) Single bent half-wavelength dipole, and (b) Two combined orthogonal bent half-wavelength dipoles.

where the expressions for parameters $D_{x'}$ and $D_{y'}$ are:

$$D_{x'} = -\int_{-\pi}^{\pi} I_e^{\varphi}(\varphi_e') e^{i\frac{2\pi}{\lambda}a\sin\theta'\cos(\varphi'-\varphi_e')}\sin\varphi_e' \mathrm{d}\varphi_e',$$
$$D_{y'} = \int_{-\pi}^{\pi} I_e^{\varphi}(\varphi_e') e^{i\frac{2\pi}{\lambda}a\sin\theta'\cos(\varphi'-\varphi_e')}\cos\varphi_e' \mathrm{d}\varphi_e'. \quad (6)$$

The relationship between $(r,\ \theta,\ \varphi)$ and $(r',\ \theta',\ \varphi')$ coordinate systems is [20]

$$\begin{aligned}
\theta' &= \arccos(\sin\theta\sin\varphi),\\
\varphi' &= \arg(\sin\theta\cos\theta - i\cos\theta),\\
(\boldsymbol{\theta}_0'\cdot\boldsymbol{\theta}_0) &= \cos\theta\cos\varphi\cos\theta'\cos\varphi'\\
&\quad -\cos\theta\sin\varphi\sin\theta' + \sin\theta\cos\theta'\sin\varphi',\\
(\boldsymbol{\theta}_0'\cdot\boldsymbol{\varphi}_0) &= -\sin\varphi\cos\theta'\cos\varphi' - \cos\varphi\sin\theta',\\
(\boldsymbol{\varphi}_0'\cdot\boldsymbol{\theta}_0) &= -\cos\theta\cos\varphi\sin\varphi' + \sin\theta\cos\varphi',\\
(\boldsymbol{\varphi}_0'\cdot\boldsymbol{\varphi}_0) &= \sin\varphi\sin\varphi'. \quad (7)
\end{aligned}$$

Hence, the radiation pattern of the combination of these two annular currents $\mathbf{j}_e^{\varphi}$ and $\mathbf{j}_e^{\varphi'}$ has the following meridional E_θ^Σ and azimuthal E_φ^Σ components:

$$E_\theta^\Sigma = E_\theta + (\boldsymbol{\theta}_0'\cdot\boldsymbol{\theta}_0)E_{\theta'} + (\boldsymbol{\varphi}_0'\cdot\boldsymbol{\theta}_0)E_{\varphi'},$$
$$E_\varphi^\Sigma = E_\varphi + (\boldsymbol{\theta}_0'\cdot\boldsymbol{\varphi}_0)E_{\theta'} + (\boldsymbol{\varphi}_0'\cdot\boldsymbol{\varphi}_0)E_{\varphi'}. \quad (8)$$

Fig. 3(a) models a half-wavelength dipole bent around a circle with radius = 0.08 λ. The corresponding gain variation for such annular current model with a=λ/4π and $I_e^{\varphi}(\varphi)$=cos(φ/2), calculated using formulae (1-3), is 3.3 dB; whereas gain variation for the bent dipole simulated in Ansys HFSS software with ideal excitation = 3.2 dB. Thus, the proposed annular current model describes the practical antenna design well. By analogy, we calculate the gain variation of the combination of two orthogonal annular currents with 90° phase difference between them (Fig. 2(c)) using formulae (1-8). The gain variation, in this case, is equal to 2.1 dB. Fig. 3(b) shows the corresponding practical design for two orthogonal bent half-wavelength dipoles with 90° phase difference, with simulated gain variation = 2.3 dB.

For the annular current models constructed by the practical half-wavelength dipoles, the bending radius effect to the radiation isotropy for the two practical models (Fig. 3) has been calculated, as shown in Fig. 4. It can be observed

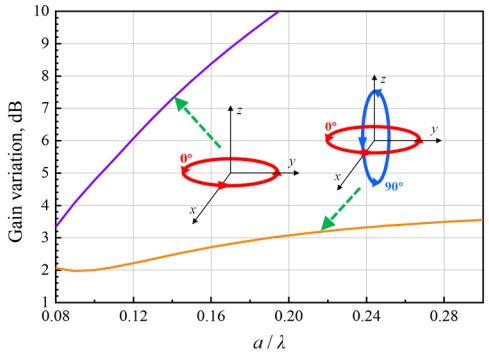

FIGURE 4. Gain variation changed with the bending radius of these two annular current models.

TABLE 1. Gain variation comparison between calculated and simulated models.

Bending radius / λ	Calculated gain variation (dB)	Simulated gain variation (dB)
0.08	2.1	2.3
0.16	2.7	2.7
0.24	3.3	3.2
∞ (Planar case)	4.0	3.9

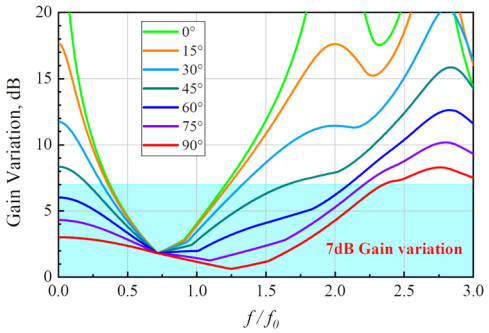

FIGURE 5. Radiation isotropy bandwidth performance for two annular currents with various phase shifts.

that the radiation isotropy generally becomes better when the radius is smaller. For the proposed annular current model, the theoretical gain variation of 2.1 dB has a better radiation isotropy performance compared with the planar type (4.0 dB). The theoretical analysis has also been validated by full-wave simulation shown in Table 1, where we can see that the simulated gain variation values matched well with the calculated ones.

Fig. 5 shows gain variations calculated from formulae (1-8) for the model in Fig. 2(c) for phase differences from 0° to 90°, normalized to f_0 (corresponding to wavelength λ = 4πa), where the annular currents have the same excitation magnitude. The best quasi-isotropic radiation pattern is achieved for 90° phase shift. Hence, the proposed annular currents model with 90° phase shift provides extremely wideband radiation isotropy. Thus, the isotropy bandwidth for the corresponding practical antenna design is limited only by its impedance bandwidth.

Impedance bandwidth limits for ESAs can be determined from Chu theory [25]. The relationship between bandwidth

and electric size for a spherical antenna can be expressed as [26]:

$$BW_{chu} = \frac{s-1}{\sqrt{s}}\left(\frac{1}{(ka)^3} + \frac{1}{ka}\right)^{-1} \quad (9)$$

where k is the wavenumber for the impedance bandwidth center frequency, a is the radius of the surrounding sphere, and s is the voltage standing wave ratio ($s = 1.925$ when return loss = 10 dB). Thus, when the electrical size $ka = 0.5$ (Fig. 3(b)), the theoretical limit of the –10 dB impedance bandwidth is 6.7%.

III. ANTENNA DESIGNS

A. ANTENNA DESIGN ON A SPHERE

Fig. 2(c) shows that two orthogonal annular half-wavelength dipoles with 90° phase difference can provide 2.1 dB gain variation, following the theory above. We validated this by full-wave simulations using ideal excitations to feed two annular half-wavelength dipoles with equal magnitude and 90° phase difference for the entire frequency band (Fig. 3(b)). However, a realistic 90° phase shifter is required for a practical antenna design, and the phase shifter may disturb antenna radiation isotropy. Thus, physically small phase shifters are strongly preferred to minimize effects on the overall radiation pattern. Therefore, we select a ring phase shifter [27], which can not only provide 90° phase shift between two annular current rings but can also help maintain wide impedance bandwidth. This design is also suitable for 3D printing process in contrast with lumped element based phase shifters [23].

Since we aim to achieve wideband anisotropy, it is possible the final phase shift may not be exactly 90° over the entire bandwidth. However, this will be acceptable since excellent isotropy can be maintained over a wide frequency band even when the phase difference is not exactly 90° (Fig. 5). The designed antenna should also offer wideband impedance bandwidth equal to the isotropic bandwidth. However, ESA maximum impedance bandwidth is limited by formula (9), i.e., 6.7% for $ka = 0.5$. This is insufficient to cover the intended application bandwidth (GSM band from 880 to 960 MHz, i.e., 8.7%). Therefore, we increased electrical size to $ka = 0.62$, which has 11.5% bandwidth limit.

Fig. 6 shows the proposed antenna design based on the annular currents model where the conductor in the simulation is lossless. The two annular dipoles are wrapped on the surface of a printed spherical shaped acrylonitrile butadiene styrene (ABS) substrate. The ring phase shifter generates the desired 90° phase shift between the annular dipoles, and incorporates two layers. The top ring layer connects to one arm of each of the orthogonal annular dipoles (Fig. 6 inset), and the bottom ring connects to the other arms. The bottom ring phase shifter has the same configuration as the top one, just rotated by 180° to form a sequential feeding network providing 0°, 90°, 180°, and 270° phases to the four

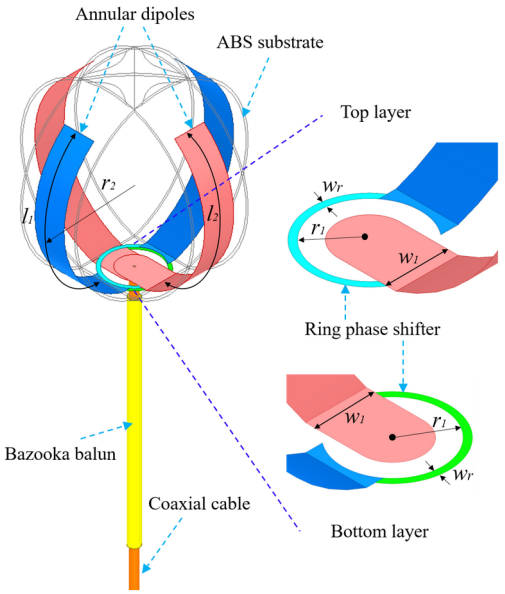

FIGURE 6. Practical antenna with wideband radiation isotropy on a sphere; l_1 = 67.6 mm, l_2 = 67.6 mm, w_1 = 11 mm, w_r = 1.2 mm, r_1 = 9 mm, and r_2 = 32 mm.

arms. This also ensures 90° phase difference is maintained between the two annular dipoles. The ring phase shifter is approximately $\lambda_g/4$ (λ_g = guided wavelength at the center frequency) long, while the width of the ring is used to adjust the impedance matching. A bazooka balun is attached to the outer surface of the coaxial cable to ensure balanced current distribution. The length of the bazooka balun is quarter-wavelength at the desired frequency of operation, which is 81 mm for this case. The distance between the dipole arms and the balun is 10 mm in the practical design. Simulations assumed 15 cm coaxial cable to model the long cable used for experiments. This is particularly for radiation pattern measurements in anechoic chambers, because long cables can affect antenna radiation isotropy. Radiation pattern isotropy deterioration due to the coaxial cable is not usually a problem for practical IoT devices since their antenna is fed by the embedded electronics. Fig. 7 shows the simulated radiation pattern for the proposed antenna, which operates at center frequency = 922 MHz. Maximum gain variation = 4.15 dB, a little higher than the ideal case (2.1 dB). This is to be expected due to including a practical phase shifter, balun and cable. Nonetheless, this is well below the 7 dB limit for quasi-isotropic radiation. Section IV compares simulated and measured results in more details.

B. ANTENNA DESIGN ON A CUBE

Although the antenna on the sphere achieved good performance, it is practically difficult to build antennas on a sphere. Fig. 8 shows a more practical quasi-isotropic antenna design on a cube. The proposed isotropic radiation theory remains valid for the cube design and variations due to shape effects can be adjusted in the simulations. Based on the Chu

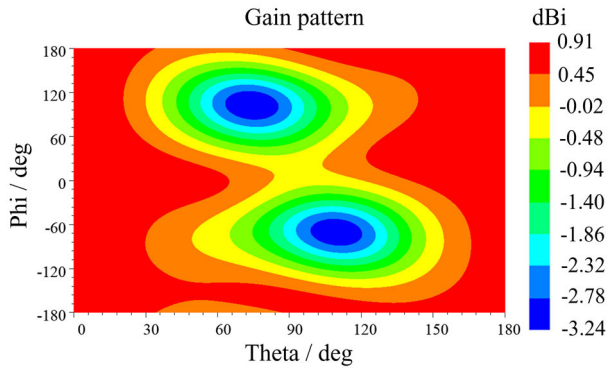

FIGURE 7. Simulated radiation pattern for the antenna on a sphere at 922 MHz.

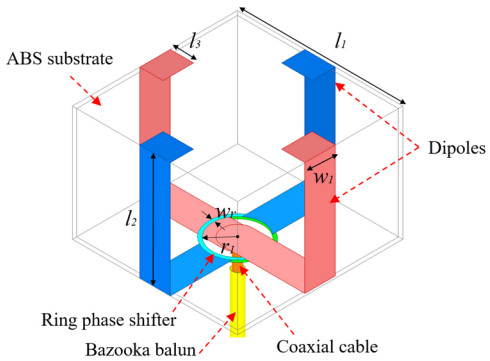

FIGURE 8. Practical antenna with wideband radiation isotropy on a cube: l_1 = 59.5 mm, l_2 = 41.5 mm, l_3 = 8.4 mm, w_1 = 11 mm, w_r = 1.2 mm, r_1 = 9 mm.

limit theory, the antenna design on a sphere has the maximum impedance bandwidth for a particular electrical size. As a result, when the radiator is moved to a cube shape from a sphere, the impedance bandwidth is decreased for the same electrical size. To maintain the radiation isotropy bandwidth, the electrical size of the cube model is increased to ka = 0.71. Fig. 9 shows the radiation pattern of the proposed cube model at center frequency = 925 MHz. Maximum gain variation = 5.29 dB, slightly larger than corresponding sphere model for the same simulation environment. This slight difference is most likely due to the sharp 90 degree bends in the cube design, causing higher current fluctuations compared with the sphere design.

IV. FABRICATION AND MEASUREMENT

Fig. 10 shows fabricated prototypes undergoing testing in an anechoic chamber, with fabrication details as follows. Substrates were 3D printed using PREFERM® ABS300 filaments on a Raise3D Pro2 printer. The spherical prototype substrate was printed in the form of a planar flexible sheet that was subsequently rolled to form a spherical shape. Metallic patterns were printed using screen printing DuPont PE819 silver paste before the substrate was rolled. In contrast, each ABS substrate surface was separately printed for the cubical shape including screen printing the metallic patterns. Substrates pieces had holes or humps to assist with assembling the complete cube structure. All 3D printed

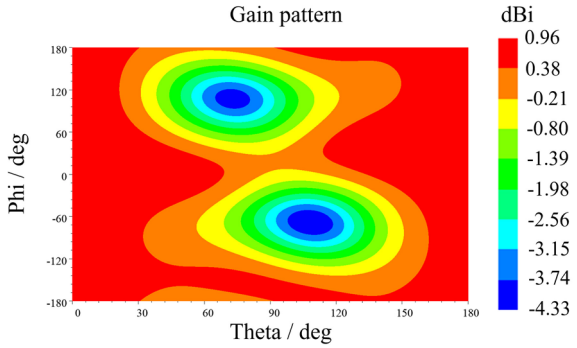

FIGURE 9. Simulated radiation pattern for the proposed antenna on a cube at 925 MHz.

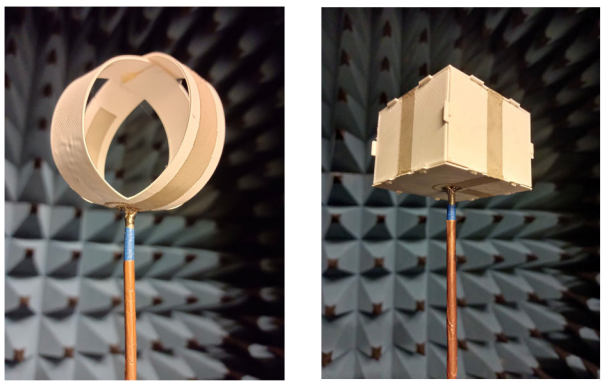

FIGURE 10. Fabricated prototype of the proposed antennas (a) sphere design. (b) cube design.

ABS substrates were 0.76 mm thick. Fully printed prototypes were assembled and placed in an oven at 70°C for two hours to cure the conductive paste. PREFERM® ABS300 filament has initial permittivity = 3 (from the manufacturer), which reduced to 2.68 after printing due to air gaps in the printed substrate. The resulting 3D printed substrate exhibited loss tangent = 0.0042 at 1 GHz, measured by impedance analyzer, which is sufficient for antenna designs in this frequency range. This fully printed process ensures very low cost and lightweight fabrication, which are highly desirable features for practical IoT applications.

Figs. 11 and 12 show impedance performance for the sphere and cube designs, respectively. Measurements were performed using a Keysight N9912A network analyzer. The proposed quasi-isotropic antenna on a sphere operates from 875 to 979 MHz with impedance bandwidth = 11.2%, very close to the Chu limit (11.5%) for an antenna with electrical size ka = 0.62. In contrast, the quasi-isotropic antenna on a cube operates from 879 to 976 MHz with 10.5% bandwidth. Measured results for both designs closely follow simulated results with only minor deviations, which is caused by the 3D printing process errors and the fabrication tolerance. Nevertheless, both designs cover the full GSM900 band (880–960 MHz).

TABLE 2. Antenna performance compared with published works.

Ref.	Isotropic synthesis approach	Antenna type	*ka**	Overall size (λ_0^2 or λ_0^3)	Impedance bandwidth (%)	Gain Deviation (dB)	Radiation isotropy bandwidth** (%) (7 dB criteria)	Efficiency (%)	Fully printed
[22]	Four L-shaped monopoles	Planar	1.13	0.36×0.36	20.82	5.75	11.5	80	No
[23]	Four L-shaped monopoles	Planar	1.02	0.23×0.23	18	4.65	6.0	87.1	No
[1]	Three electric dipoles	3D	1.16	0.32×0.13×0.13	8.9/33.3	8.8/9.8	Gain variation > 7 dB	NA/NA	Yes
[2]	Three electric dipoles	3D	2.62	0.48×0.48×0.48	30	93% 7dB isotropy	Gain variation > 7 dB	NA	No
[21]	Two cross dipoles	Planar	0.82	0.26×0.26	11	6.67	3.3	NA	No
[20]	Triple Current Line Sources	Planar	0.93	0.21×0.21	3	3.6	3	NA	No
[9]	Orthogonal electric and magnetic dipoles	Planar	0.49	$\pi\times0.078^2$	1.0/2.2	5.83/8.24	1.0/2.2	63/91	No
[6]	Orthogonal electric and magnetic dipoles	3D	0.49	0.1×0.1×0.34	2.9	3.3	2.9	NA	Yes
[13]	Orthogonal electric and magnetic dipoles	3D	1.05	0.22×0.22×0.12	7.3	3.4	<7.3	95	No
This work	Annular currents on a sphere	3D	0.62	$4\pi/3\times0.098^2$	11.2	4.6	11.2	90.6	Yes
This work	Annular currents on a cube	3D	0.71	0.18×0.18×0.13	10.5	4.8	10.5	87.3	Yes

* *ka* refers to the electrical size of radiated structure only.
** The radiation isotropy bandwidth refers to the effective bandwidth within the impedance bandwidth.

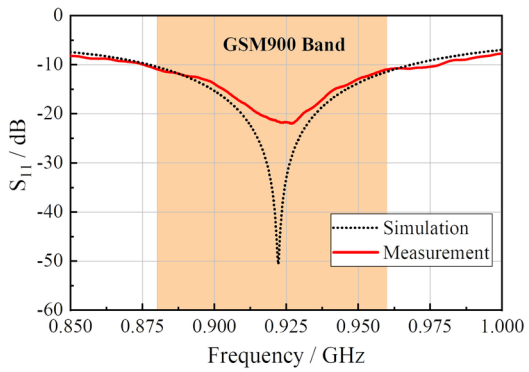

FIGURE 11. Simulated and measured S_{11} for the proposed antenna on a sphere.

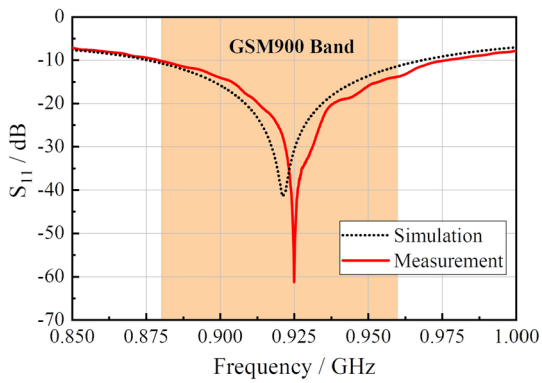

FIGURE 12. Simulated and measured S_{11} for the proposed antenna on a cube.

Figs. 13 and 14 compared measured and simulated radiation performance for the two fabricated antennas, respectively, measured in a Satimo StarLab anechoic chamber. Measured results follow the simulation trends well, with some variations over the bandwidth. Nonetheless, both designs have gain variation < 7 dB across the entire bandwidth. These measurements were taken using the long feeding cable and balun. Although these were simulated, the actual cases have various practical imperfections that will cause deviations between simulated and measured results. Practical IoT applications feed their antennas from the internal requisite electronics, rather than requiring coaxial cable and balun, and hence one could expect better agreement for that case. Fig. 15 shows simulated and measured efficiencies for the two fabricated prototypes (Eff = P_r/P_{in}, where P_r and P_{in} are the radiated power and input power of an antenna, respectively). Measured results show the antennas achieved average radiation efficiency = 90.6% and 87.3% within their impedance bandwidth, respectively. This is an excellent result for a fully printed electrically small antenna.

Table 2 compares the wideband radiation isotropy performance of fabricated prototype with previous quasi-isotropic antenna designs. Some planar quasi-isotropic antennas have been proposed [9], [13], [20], [21], but these antennas did not consider wideband radiation isotropy and typically have narrow radiation isotropy bandwidths (≈ 3%).

Two 3D AiP designs generated quasi-isotropic radiation patterns [1], [2], but the orthogonal electric dipoles based designs only generated very narrow band isotropy, and they were electrically large. One 3D antenna with a

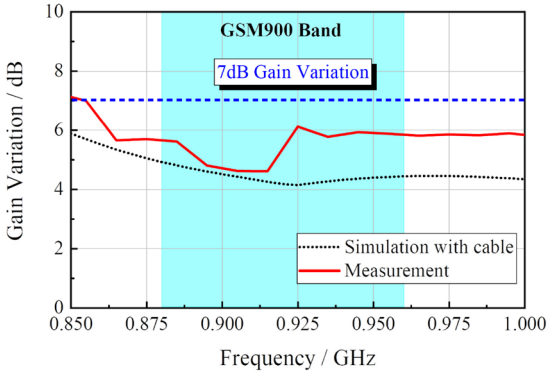

FIGURE 13. Simulated and measured gain variation with respect to frequency for the proposed antenna on a sphere.

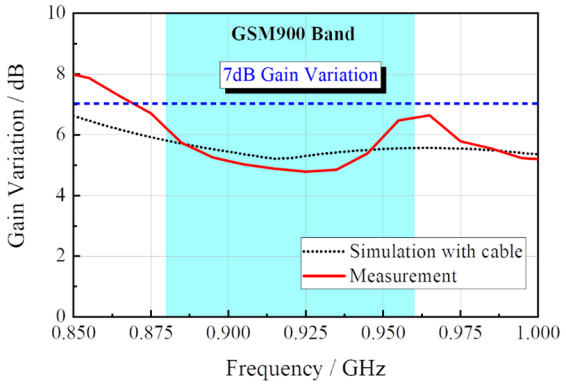

FIGURE 14. Simulated and measured gain variation with respect to frequency for the proposed antenna on a cube.

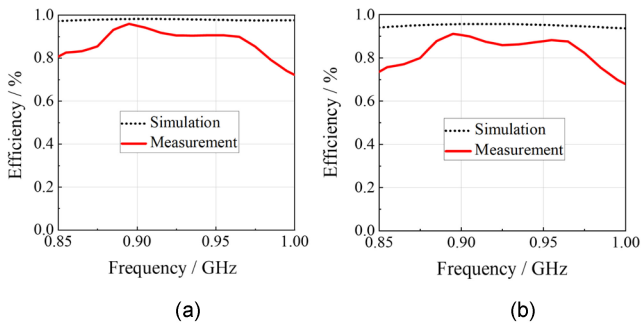

FIGURE 15. Simulated and measured efficiency with respect to operating frequency for fabricated prototype antenna (a) on a sphere and (b) on a cube.

quasi-isotropic radiation pattern [6] was electrically small, but also suffers from narrow bandwidth. Therefore, in terms of the radiation isotropy at a single frequency, our measured gain deviation is more excellent compared with some of its counterparts [1], [2], [9], [21], [22], [23]. Although those works have lower measured gain deviation [6], [13], [20], they show very narrow bandwidth. Considering the quasi-isotropic radiation pattern in a wide band, only two previous studies achieved wide radiation isotropy bandwidths = 11.5% and 6%, respectively [22], [23], based on four rotated L-shaped monopoles. However, they are electrically large compared with the proposed design and planar, hence somewhat unsuitable for 3D AiP, where the electronics can be embedded in the antenna. They were also not realized using low cost printing process and offered no theoretical approach to design isotropic antennas. By contrast, we present a novel theoretical approach to design quasi-isotropic antennas with wideband performance. Two fabricated antennas inspired by the theoretical model demonstrate wideband impedance bandwidth and radiation isotropy bandwidth of 11.2% and 10.5% that are close to *Chu-limit* (11.5%), with compact sizes (ka = 0.62 and 0.71) and high radiation efficiency (∼90%).

V. CONCLUSION

In our work, two orthogonal annular currents with 90° phase differences were proposed as the practically applicable quasi-isotropic synthesis method with wideband radiation isotropy performance. We fabricated two fully printed ESAs based on the proposed annular currents model, covering the GSM900 band for IoT applications. Fabricated ESAs on a sphere and a cube exhibited radiation isotropy bandwidths > 10% with small electrical sizes ka = 0.62 and 0.71, respectively, which are suitable for miniaturized IoT devices. The designs presented in this paper have been fully printed and despite being electrically small and realized through low-cost printing methods, they demonstrate measured radiation efficiencies of around 90%. In conclusion, the proposed theory, the design methodology, excellent radiation isotropy performance with an electrically small size, and low cost fully printed fabrication that is suitable for mass manufacturing make this work attractive for a number of IoT applications that require orientation insensitive communication for a large bandwidth. The annular currents model has shown good matching with folded dipoles antennas on a sphere. Thus, it can be used for designing larger and more complex folded dipoles antennas, which will be able to provide larger impedance and radiation isotropy bandwidths. Also, such the ESA is a good candidate for designing an element of adaptive conformal antenna arrays.

REFERENCES

[1] Z. Su, K. Klionovski, R. M. Bilal, and A. Shamim, "A dual band additively manufactured 3-D antenna on package with near-isotropic radiation pattern," *IEEE Trans. Antennas Propag.*, vol. 66, no. 7, pp. 3295–3305, Jul. 2018.

[2] Z. Su, K. Klionovski, H. Liao, Y. Chen, A. Z. Elsherbeni, and A. Shamim, "Antenna-on-package design: Achieving near-isotropic radiation pattern and wide CP coverage simultaneously," *IEEE Trans. Antennas Propag.*, vol. 69, no. 7, pp. 3740–3749, Jul. 2021.

[3] Z. Su, K. Klionovski, H. Liao, W. Li, and A. Shamim, "A fully-printed 3D antenna with 92% quasi-isotropic and 85% CP coverage," *IEEE Trans. Antennas Propag.*, vol. 70, no. 9, pp. 7914–7922, Sep. 2022, doi: 10.1109/TAP.2022.3168688.

[4] C. M. Kruesi, R. J. Vyas, and M. M. Tentzeris, "Design and development of a novel 3-D cubic antenna for wireless sensor networks (WSNs) and RFID applications," *IEEE Trans. Antennas Propag.*, vol. 57, no. 10, pp. 3293–3299, Oct. 2009.

[5] M. F. Farooqui, C. Claudel, and A. Shamim, "An inkjet-printed buoyant 3-D Lagrangian sensor for real-time flood monitoring," *IEEE Trans. Antennas Propag.*, vol. 62, no. 6, pp. 3354–3359, Jun. 2014.

[6] H. Liao, Q. Zhang, M. A. Karimi, Y. Kuo, N. Mishra, and A. Shamim, "An additively manufactured 3-D antenna-in-package with quasi-isotropic radiation for marine animals monitoring system," *IEEE Antennas Wireless Propag. Lett.*, vol. 18, no. 11, pp. 2384–2388, Nov. 2019.
[7] M. B. Arboleda, K. Klionovski, S. Zhen, and A. Shamim, "Orientation aware intelligent 3-D cubic antenna system with automated radiation pattern reconfigurability," *IEEE Open J. Antennas Propag.*, vol. 3, pp. 812–823, 2022.
[8] S. Lee, G. Tewolde, and J. Kwon, "Design and implementation of vehicle tracking system using GPS/GSM/GPRS technology and smartphone application," in *Proc. IEEE World Forum Internet Things (WF-IoT)*, Mar. 2014, pp. 353–358.
[9] S. M. Radha, G. Shin, W. Kim, S. I. H. Shah, and I.-J. Yoon, "Design and verification of an electrically small, extremely thin dual-band quasi-isotropic antenna," *IEEE Antennas Wireless Propag. Lett.*, vol. 19, no. 12, pp. 2482–2486, Dec. 2020.
[10] J.-H. Kim and S. Nam, "Design of a compact dualband quasi-isotropic antenna," *Electron. Lett.*, vol. 53, no. 8, pp. 515–516, Apr. 2017.
[11] H. Tang et al., "A low-profile flexible dual-band antenna with quasi-isotropic radiation patterns for MIMO system on UAVs," *IEEE Antennas Wireless Propag. Lett.*, vol. 22, no. 1, pp. 49–53, Jan. 2023.
[12] C. M. A. Niamien, "Single-feed planar multiband quasi-isotropic antennas through collocating and co-design approaches," *IEEE Trans. Antennas Propag.*, vol. 71, no. 4, pp. 2974–2988, Apr. 2023.
[13] Y. Pan, K. W. Leung, and K. Lu, "Compact quasi-isotropic dielectric resonator antenna with small ground plane," *IEEE Trans. Antennas Propag.*, vol. 62, no. 2, pp. 577–585, Feb. 2014.
[14] P. F. Hu, Y. M. Pan, X. Y. Zhang, and B. J. Hu, "A compact quasi-isotropic dielectric resonator antenna with filtering response," *IEEE Trans. Antennas Propag.*, vol. 67, no. 2, pp. 1294–1299, Feb. 2019.
[15] Y. Xu, Y. Zhu, S. Wen, and Y. Dong, "Planar quasi-isotropic antenna and its implementation of filtering response," *IEEE Antennas Wireless Propag. Lett.*, vol. 20, no. 12, pp. 2407–2411, Dec. 2021.
[16] J. Ouyang, Y. M. Pan, S. Y. Zheng, and P. F. Hu, "An electrically small planar quasi-isotropic antenna," *IEEE Antennas Wireless Propag. Lett.*, vol. 17, no. 2, pp. 303–306, Feb. 2018.
[17] Y. Wang et al., "Design of low-cost, flexible, uniplanar, electrically small, quasi-isotropic antenna," *IEEE Antennas Wireless Propag. Lett.*, vol. 18, no. 8, pp. 1646–1650, Aug. 2019.
[18] S. Long, "A combination of linear and slot antennas for quasi-isotropic coverage," *IEEE Trans. Antennas Propag.*, vol. 23, no. 4, pp. 572–576, Jul. 1975.
[19] H. Matzner and K. T. McDonald, "Isotropic radiators," Dec. 2003, *arXiv:physics/0312023v1*.
[20] P. Liu and Y. Li, "Quasi-isotropic radiation pattern synthesis using triple current line sources," *IEEE Trans. Antennas Propag.*, vol. 68, no. 12, pp. 8150–8155, Dec. 2020.
[21] G. Pan, Y. Li, Z. Zhang, and Z. Feng, "Isotropic radiation from a compact planar antenna using two crossed dipoles," *IEEE Antennas Wireless Propag. Lett.*, vol. 11, pp. 1338–1341, 2012.
[22] C. Deng, Y. Li, Z. Zhang, and Z. Feng, "A wideband isotropic radiated planar antenna using sequential rotated L-shaped monopoles," *IEEE Trans. Antennas Propag.*, vol. 62, no. 3, pp. 1461–1464, Mar. 2014.
[23] Y. Zhang and Y. Li, "Wideband isotropic antenna with miniaturized ground for enhanced 3 dB coverage ratio," *IEEE Antennas Wireless Propag. Lett.*, vol. 21, no. 6, pp. 1253–1257, Jun. 2022.
[24] A. L. Drabkin and V. L. Zuzenko, *Antenna-Feeder Devices*. Moscow, Russia: Soviet Radio, 1961.
[25] L. J. Chu, "Physical limitations of omni-directional antennas," *J. Appl. Phys.*, vol. 19, no. 12, pp. 1163–1175, Dec. 1948.
[26] Z. Wang, S. Liu, and Y. Dong, "Electrically small, low-Q, wide beam-width, circularly polarized, hybrid magnetic dipole antenna for RFID application," *IEEE Trans. Antennas Propag.*, vol. 69, no. 10, pp. 6284–6293, Oct. 2021.
[27] J.-W. Baik, W.-S. Yoon, K. J. Lee, W.-S. Yoon, T.-H. Lee, and Y.-S. Kim, "Circularly polarised printed crossed dipole antenna with broadband axial ratio," *Election. Lett.*, vol. 44, no. 13, pp. 785–786, 2008.

RUIQI WANG received the B.S. degree in electronic engineering from the University of Electric Science and Technology of China, Chengdu, China, in 2021, and the M.S. degree in electrical and computer engineering from the King Abdullah University of Science and Technology, Thuwal, Saudi Arabia, in 2022, where he is currently pursuing the Ph.D. degree. His current research interests include antenna radiation pattern synthesis and reconfigurable intelligent surfaces.

KIRILL KLIONOVSKI received the Ph.D. degree in radiophysics from the Institute of Radioengineering and Electronics, Russian Academy of Sciences, Moscow, in 2015.

His current research interests include orientation insensitive antennas and applied electromagnetics.

ATIF SHAMIM (Senior Member, IEEE) received the M.S. and Ph.D. degrees in electrical engineering from Carleton University, Ottawa, ON, Canada, in 2004 and 2009, respectively. He was an NSERC Alexander Graham Bell Graduate Scholar with Carleton University from 2007 to 2009 and an NSERC Postdoctoral Fellow with Royal Military College Canada from 2009 to 2010 and the King Abdullah University of Science and Technology (KAUST), Thuwal, Saudi Arabia. In August 2010, he joined the Electrical Engineering Program, KAUST, where he is currently a Professor and the Principal Investigator of the IMPACT Lab. He was an Invited Researcher with the VTT Micro-Modules Research Center, Oulu, Finland, in 2006. He is an author of one book, three book chapters, and 250 publications; an inventor on 30 patents; and has given 70 invited talks at various international forums. His research interests include innovative antenna designs and their integration strategies with circuits and sensors for flexible and wearable wireless sensing systems through a combination of CMOS and additive manufacturing technologies. He was the recipient of the Best Paper Awards in IEEE IMS 2016, IEEE MECAP 2016, IEEE EuWiT 2008; the first prize in the IEEE IMS 2019 3MT competition; the finalist/honorable mention prizes in IEEE APS Design Competition 2020, IEEE APS 2005, IEEE IMS 2014, IEEE IMS 2017 (3MT competition); and the R. W. P. King IEEE Award for journal papers in IEEE TAP 2017 and 2020. He was given the Ottawa Centre of Research Innovation (OCRI) Researcher of the Year Award, Canada, in 2008. His work on wireless dosimeter won the ITAC SMC Award at Canadian Microelectronics TEXPO in 2007. He also was the recipient of numerous business-related awards, including 1st Prize in Canada's National Business Plan Competition and the OCRI Entrepreneur of the Year Award in 2010 and the Kings Prize for the best innovation of the year in 2018 for his work on sensors for the oil industry. He is a member of the IEEE APS Measurements Committee and the IEEE MTT Microwave Control Techniques Committee, founded the first IEEE AP/MTT chapter in Saudi Arabia in 2013 and served on the editorial board of IEEE TRANSACTIONS ON ANTENNAS AND PROPAGATION from 2013 to 2019, and the Guest Editor for IEEE AWPL Special issue in 2019. He is currently an Associate Editor for IEEE JOURNAL OF ELECTROMAGNETICS, RF AND MICROWAVES IN MEDICINE AND BIOLOGY. He has been selected as the Distinguished Lecturer for AP-S since 2022.